



## Visible-light-driven inactivation of *Escherichia coli* K-12 over thermal treated natural pyrrhotite



Dehua Xia<sup>a,1</sup>, Yan Li<sup>b,1</sup>, Guocheng Huang<sup>a</sup>, Chi Ching Fong<sup>a</sup>, Taicheng An<sup>c,\*\*</sup>, Guiying Li<sup>c</sup>, Ho Yin Yip<sup>a</sup>, Hunjun Zhao<sup>d</sup>, Anhuai Lu<sup>b,e</sup>, Po Keung Wong<sup>a,c,\*</sup>

<sup>a</sup> School of Life Sciences, The Chinese University of Hong Kong, Shatin, NT, Hong Kong SAR, China

<sup>b</sup> The Key Laboratory of Orogenic Belts and Crustal Evolution, School of Earth and Space Sciences, Peking University, Beijing 100871, China

<sup>c</sup> State Key Laboratory of Organic Geochemistry, Guangzhou Institute of Geochemistry, Chinese Academy of Sciences, Guangzhou 510640, China

<sup>d</sup> Centre for Clean Environment and Energy, Gold Coast Campus, Griffith University, Queensland 4222, Australia

<sup>e</sup> School of Geoscience and Info-Physics, Central South University, Changsha 410083, China

### ARTICLE INFO

#### Article history:

Received 24 November 2014

Received in revised form 2 March 2015

Accepted 15 April 2015

Available online 17 April 2015

#### Keywords:

Natural pyrrhotite

Bacterial inactivation

Annealing

Mineral photocatalyst

### ABSTRACT

A novel magnetic natural pyrrhotite (NP) mineral photocatalyst was developed and modified by thermal treatment. Their photocatalytic activity were evaluated by photocatalytic inactivation of *Escherichia coli* K-12 under visible light. As compared to NP, the annealed NP was found to exhibit a remarkable enhanced bactericidal activity. Among them, the NP treated at 600 °C in air (NP600) had the highest activity and the inactivation rate was nearly 3 times higher than that of untreated NP. The X-ray diffraction (XRD) spectra indicated the mineral phase of NP600 transformed to mixed crystallite phases of hematite-pyrite (Fe<sub>2</sub>O<sub>3</sub>-FeS<sub>2</sub>) composite. Thus, the enhanced photocatalytic performance was mainly attributed to the formation of Z-scheme photocatalysis system composed of hematite and pyrite, which could improve the electron-hole separation efficiency and the bactericidal efficiency. Scavenger study demonstrated that the dominant bactericidal agent changed from superoxide radical ( $\cdot\text{O}_2^-$ ) for NP to hydroxyl radical ( $\cdot\text{OH}$ ) for NP600. Moreover, vibrating sampling magnetizer (VSM) analysis revealed that the saturated magnetism of NP after thermal anneal was enhanced. The strong magnetic behavior of thermal treated NP enabled the magnetic recovery of photocatalysts after liquid phase reaction. In addition, NP600 was more stable than untreated NP and with lower metal ion leakage even after four reaction cycles. This work supplied a cost-effective natural mineral-based photocatalyst and an efficient modification strategy to extend the application field of natural minerals in water disinfection.

© 2015 Elsevier B.V. All rights reserved.

### 1. Introduction

Naturally occurring semiconductor minerals are earth-abundant and able to perform visible-light-driven (VLD) photocatalytic activity for environmental remediation in several aspects: to reduce heavy metal, to decompose organic pollutants, and even to inactivate bacterial cells [1–4]. The VLD photocatalytic activity of these materials is mainly attributed to the modification of band structure by impurity elements and lattice defects as compared to their synthetic counterparts [3]. Recently developed natural magnetic sphalerite (NMS) could efficiently inactivate *Escherichia coli* K-12, due to the major bactericidal agent

of conduction band  $e^-$  induced  $\cdot\text{O}_2^-$  [5]. Compared with synthetic VLD photocatalysts, natural magnetic VLD minerals are more readily obtained as magnetically separable photocatalysts and more feasible to be recycled, indicating a stronger potential for environmental applications [5]. Consequently, the selection and development of this type of photocatalysts are urgently needed.

Pyrrhotite (Fe<sub>1-x</sub>S) with good optical absorption ability ( $\alpha = 6 \times 10^5 \text{ cm}^{-1}$ ) has been widely used in solar cell and photovoltaics [6,7], and developed as a photocatalyst for pollutant degradation [8–10]. But in mineral processing industry, the economic value of natural pyrrhotite was considered to be not as high as other sulfides. Even sometimes it was abandoned as a waste and discarded in the open air due to the oversupply in the sulphuric acid market, giving rise to serious environmental problems of acid mine drainage [11,12]. Therefore, it is very meaningful to investigate and develop its photocatalytic ability to control the outbreak of water-borne microorganisms [12].

\* Corresponding author. Tel.: +852 39436383; fax: +852 26035767.

\*\* Corresponding author. Tel.: +86 20 85291501; fax: +86 20 85290706.

E-mail addresses: [antc99@gig.ac.cn](mailto:antc99@gig.ac.cn) (T. An), [pkwong@cuhk.edu.hk](mailto:pkwong@cuhk.edu.hk) (P.K. Wong).

<sup>1</sup> Equal contribution.

However, previous studies showed the practical use of natural minerals was limited by the low photocatalytic activity and possible release of potential hazardous ions. For example, NMS need 6 h irradiation to totally inactivate 7 Log<sub>10</sub> cfu/mL *E. coli* under the optimized condition, accompanied with 0.6 ppm Zn<sup>2+</sup> released into the liquid [5]. Thermal modification of natural minerals may be a good choice to address the above two problems simultaneously, because heating can repair the lattice defects and improve the crystalline degree [13], amplify the crystalline size [14], transform the mineral phase [15–18], and possibly remove the impurities [19–21].

In this study, we have developed a magnetic natural pyrrhotite (NP) for photocatalytic disinfection of water sample. To further improve its photocatalytic efficiency, the NP sample was thermally treated and the physiochemical properties were characterized to better understand its photocatalytic disinfection mechanism. Scavenger studies were also conducted to detect the major reactive species (RS) responsible for photocatalytic inactivation of bacteria. In order to investigate the stability of thermally treated NP for long-term application, the photocatalytic performance of the samples in multi-cycle experiments were conducted and the released metal ions were quantitatively analyzed. The good VLD photocatalytic activity and stability of thermally treated NP will attract great interests in developing natural mineral-based environmental material applied for water treatment.

## 2. Experimental

### 2.1. Materials and characterization

Pristine NP was collected from a mining site in China. The raw mineral was crushed by machine, washed with tap water, dried under ambient condition, and then selected by an electromagnetic and gravity separator. Before use, the picked NP was sieved through 300-mesh to obtain final powders with size between 38 and 75 μm. The X-ray diffraction (XRD) spectra of as-prepared NP were recorded on the DMAX-2400 diffractor (Rigaku, Japan, Cu Kα, λ = 0.15406 nm) with 40 kV accelerating voltage and 15 mA current. The morphologies of the calcined products were characterized by a scanning electron microscopy (FESEM, FEI, Quanta 400 FEG) equipped with an energy-dispersive X-ray (EDX) spectrometer. The chemical compositions of several randomly selected mineral particles were characterized by electron microprobe analyses (EMPA, JEOL JXA 733) at China University of Geosciences (Beijing). The standards employed were natural minerals from the Society of the Plastics Industry, Inc. (SPI). The powder samples were dispersed by ultra-sonication in ethanol, and then dropped on a silicon wafer for SEM observation. UV–visible diffuse reflection spectra (DRS) pattern of NP were recorded by a UV–visible spectrophotometer (Lambda 950) with an integral-sphere attachment range from 300 to 800 nm and BaSO<sub>4</sub> was used as a reference. The measurement of magnetic properties of NP powder was conducted by vibrating sample magnetometer (VSM-7300, Quantum design, Lakeshore, USA) at 25 °C.

### 2.2. Thermal treatment process

During the pre-heat process in air, 1 g of pristine NP powder was transferred into alumina porcelain crucible and then heated in a high-temperature tubular furnace (Vulcan 3-1750, U.S.A) from room temperature to the designated temperature ranging from 200 to 800 °C with a heating rate of 10 °C/min. While heating in argon atmosphere, NP powder was transferred into another furnace (OTF-1200X, KJMTI, Hefei, China) with a continuous argon flow of 0.5 L/min and then heated to the designated temperature with a heating rate of 10 °C/min. Similarly, all the samples were

maintained at the designated temperature for 2 h, and then cooled down to room condition. Samples annealed in air were labeled as NP200, NP400, NP600 and NP800 for respective heating temperatures, while those annealed in argon atmosphere were labeled as NP200A, NP400A, NP600A and NP800A for respective heating temperatures.

### 2.3. Photocatalytic inactivation process

50 mL mixture suspension of 1 g/L as-prepared NP and 10<sup>7</sup> cfu/mL *E. coli* K-12 in a flask was put into a photocatalytic reactor and vigorously stirred by a plastic stirrer. Six fluorescent tubes (FTs) (15 W, VELOX, Thailand) were installed on top of the reactor as light source, and the VL and UV intensities were determined by a light meter (LI-COR, Lincoln, Nebraska, USA) and an UVX digital radiometer (UVP, Upland, California, USA), respectively. Aliquot samples were collected at different time intervals and diluted serially with sterilized saline (0.9% NaCl solution), then immediately spread on the Nutrient Agar (Lab M, Lancashire, UK) plate. After that, all the plates were incubated at 37 °C for 24 h to obtain the survival cell numbers. All glassware and accessories utilized in the experiment were autoclaved at 121 °C for 20 min in advance. Light control (without NP) and dark control (without light) were conducted in parallel to study whether photolysis or NP alone could cause the cell death [5,22–24].

### 2.4. Fluorescence spectroscopy and analysis of ions leakage

During the photocatalytic treatment process, 1 mL of solution containing photocatalyst at the optimal calcined temperature and *E. coli* K-12 suspension were collected at several time intervals, concentrated to 0.1 mL by centrifuge and then stained with the dye mixture of LIVE/DEAD BacLight Bacterial Viability Kit (L7012, Molecular Probes, Inc. Eugene, OR) [5,23,24]. The dye mixture reagent consisted of SYTO 9 and propidium iodide (PI) dye was diluted in 5 mL of deionized water. SYTO 9 labels all the bacterial cells whereas PI penetrates only those with damaged cell membranes. After being incubated at 25 °C in the dark for 15 min, the prepared samples were pipetted onto a cover-slip and observed by a light microscope (Nikon ECLIPSE 80i, Japan), which was equipped with a filter block NUV-2A consisting of excitation filter Ex 400–680 (Nikon, Japan) and Spot-K slider CCD camera (Diagnostic Instruments, Inc. USA). Metal ions bleaching from NP and K<sup>+</sup> releasing from the cell during the photocatalytic inactivation of bacteria were measured by a polarized Zeeman atomic absorption spectrophotometer (AAS) (Hitachi Z-2300, Japan).

### 2.5. Scanning electron microscopy

Following the procedures of previous studies [23,24], at several time intervals, aliquot samples were extracted from the photocatalytic reactor and then transferred onto acid-washed and poly-lysine coated cover-slips. After pre-fixation in 5% glutaraldehyde solution for 1 h, the specimen was washed twice by 0.1 M PBS at pH 7 and then post-fixed with 2% osmium tetroxide (E.M. grade, Electron Microscopy Sciences, Fort Washington, PA, USA) in dark for 1 h. Then the specimens were washed twice by distilled water before further soaked and dehydrated in a gradient series of ethanol (50, 60, 70, 80, 90, 95 and 100%, and each for 10 min), and then critical point dried within CO<sub>2</sub> atmosphere. The dried specimens were mounted on stubs and sputter-coated with gold and palladium. Finally, the prepared samples were observed by a scanning electron microscope (Joel-JSM-6301-F) at an accelerating voltage of 5 kV.

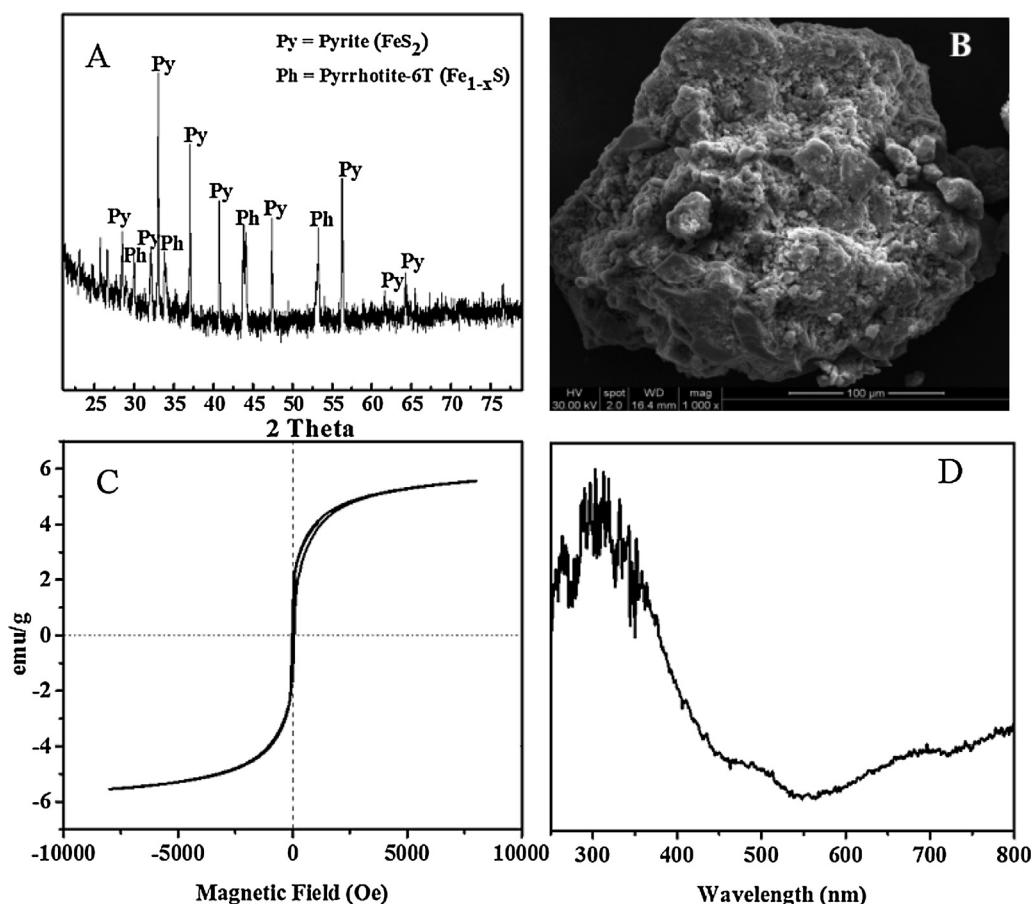


Fig. 1. XRD, SEM, magnetic loop and UV-vis DRS spectra of pristine NP.

## 2.6. Statistical analysis

Results are expressed as mean  $\pm$  standard deviation. For all the photocatalytic bacterial inactivation experiments, the differences between the survival cells at different exposure times or with scavenger chemicals were determined using repeated-measures ANOVA. In addition, the differences of the measured parameters were determined using one-way ANOVA. All the statistical analyses were carried out using SPSS 16.0 statistical software (IBM Corporation, Somers, NY), and  $p < 0.01$  was considered to be statistically significant.

## 3. Results and discussion

### 3.1. Photocatalytic inactivation performance

#### 3.1.1. Inactivation kinetics

Different from the pure material, natural pyrrhotite always occurred with impurity mineral phases. The most common associated mineral of pyrrhotite is pyrite ( $\text{FeS}_2$ ), which is also a semiconductor mineral. XRD patterns indicate the pristine NP sample is composed of mixed phases of pyrrhotite-6T ( $\text{Fe}_{1-x}\text{S}$ , PDF 29-0725) and pyrite ( $\text{FeS}_2$ , PDF 42-1340) (Fig. 1A). Many mechanically ground fractures are observed on the surface of NP by SEM (Fig. 1B). Based on the results of EMPA in Table S1 (Supporting Information), the chemical formula of NP can be expressed as  $(\text{Fe}_{0.8656}\text{Ni}_{0.00045}\text{Mn}_{0.0018}\text{Cu}_{0.002}\text{Pd}_{0.0028}\text{Zn}_{0.0015}\text{Cd}_{0.0001}\text{Co}_{0.0002})_{0.875}\text{S}$ . UV-vis spectrum (Fig. 1D) shows a broad absorption band in the range of 300–800 nm, indicating both UV- and visible-light response of the natural mineral. The viability of *E. coli*

during the photocatalytic experiments with pristine and annealed NP are shown in Fig. 2. Obviously, pristine NP can inactivate  $2\text{-log}_{10}$  cfu/mL *E. coli* K-12 after 4 h irradiation. Direct photolysis of *E. coli* K-12 without any photocatalyst is negligible because the cell density remained relatively constant during the whole experimental period (Fig. S1). The observation of very slight reductions of cell density in dark with pristine and heat treated NP samples (Fig. S1) could be attributed to the adsorption of cells onto the mineral surface [25]. Therefore, the inactivation of *E. coli* K-12 was due to the VLD photocatalysis of pristine NP. As observed in Fig. 2, *E. coli* K-12 could also be effectively inactivated by the photocatalysis of almost all thermally treated NP. As compared to the pristine NP, obvious enhancement of cell inactivation rates were observed for NP400 and NP600, while a surprising drop of the inactivation efficiency ( $1\text{-log}_{10}$  cfu/mL) was observed for NP800. Specially, NP600 behaved the best photocatalytic capability on disinfection of *E. coli* K-12, that totally  $7\text{-log}_{10}$  cfu/mL cells were inactivated within 4 h. In argon atmosphere, the cells loss level increased from  $2\text{-log}_{10}$  cfu/mL (NP200A) to  $3\text{-log}_{10}$  cfu/mL (NP600A), indicating a slight enhancement of cell inactivation efficiency by annealed NP samples. Similar to NP800, the NP800A behaved even worse photocatalytic activity than the pristine NP, and almost no cell loss was observed in the inactivation pattern of NP800A.

It is interesting to note that the inactivation kinetics were modelled with a first-order decay of viability, followed by the presence of a tailing phase in which liberated intracellular components competing with the intact cell for the photocatalytic attack. The results can be fitted well by Eq. (1) (a model proposed by Geraerd et al. [26]):

$$N(t) = (N_0 - N_{\text{res}}) \times \exp(-k_{\text{max}} \times t) + N_{\text{res}} \quad (1)$$

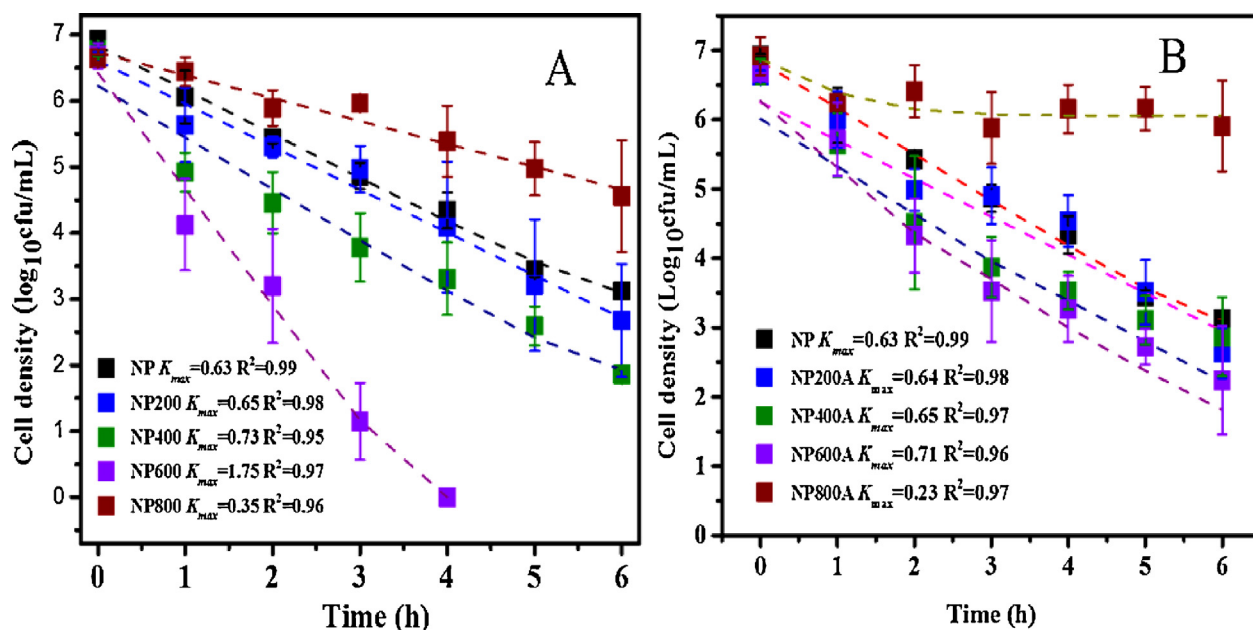


Fig. 2. Photocatalytic inactivation efficiencies of *E. coli* K-12 by pristine NP and treated NP at different temperature in air (A) and argon (B). Light intensity: visible light = 3.58 mW/cm<sup>2</sup>, UVA = 0.03 mW/cm<sup>2</sup>, UVB = 0.005 mW/cm<sup>2</sup>, UVC = 0.002 mW/cm<sup>2</sup>.

Where  $N(t)$  and  $N(0)$  were related to the survival number of cells (log, in cfu) at different irradiation time equal to  $t$  and  $0$ ;  $k_{max}$  denoted the inactivation rate and  $N_{res}$  was the residual number of cells (log, in cfu); exp is the natural logarithm equal to 2.71828. With the increasing temperature, the fitted values of  $k_{max}$  (Inset of Fig. 1) increased from 0.63 to 1.75 for air annealed NP, while it showed only limited increase from 0.63 to 0.71 for argon annealed NP. These results further support that thermal treatment in air is an efficient strategy for improving the photocatalytic activity of NP. Moreover, oxygen may play a critical role in the thermal modification process, which enabled the oxidation reaction and possibly resulted in the phase transformation of NP.

### 3.1.2. Membrane permeability changes and bacterial decomposition

As discussed above, the photocatalytic inactivation rate of NP600 is almost 3 times faster than that of NP. The membrane integrity of *E. coli* cells during the inactivation with untreated NP and NP600 was monitored by BacLight™ fluorescent kit and imaged by light microscope (Fig. S2A). In the VL-NP600 system, the untreated intact cells only accumulated SYTO 9 to fluoresce green, while red fluorescent cells with compromised membranes

increased with prolonged treatment due to significant penetration of propidium iodide (PI). All bacterial cells were stained red at 4 h, suggesting that the cell membrane integrity of all the cells was lost. In contrast, the permeabilization of the cells with NP was much slower, with most cells remaining green even after 4 h (Fig. S2B). The results indicated that the quicker peroxidation of cell membranes might be due to the more serious oxidative stress induced by NP600. Bosshard et al. [27] reported that increased membrane permeability would expose more of the membrane associated with proteins like ATPase and respiratory enzymes to be decomposed, and thus decrease the membrane potential with shutting the substrate transport process. The elevated K<sup>+</sup> leakage from cytoplasm is another evidence to reflect the relative order of increased membrane permeability [5,22,23]. In well accordance with the inactivation progress, the concentration of K<sup>+</sup> in NP600 photocatalytic system sharply increased within the initial 2 h, while it maintained stable thereafter (Fig. S3). The results further supported that the bacterial cells were more susceptible to be attacked by the powerful ROSs from NP600. Moreover, the damage of cell membranes motivates us to visually observe the cell destruction directly by SEM (Fig. 3). Aggravating shrink and rupture in the envelope of most cells in the presence of NP600, which was

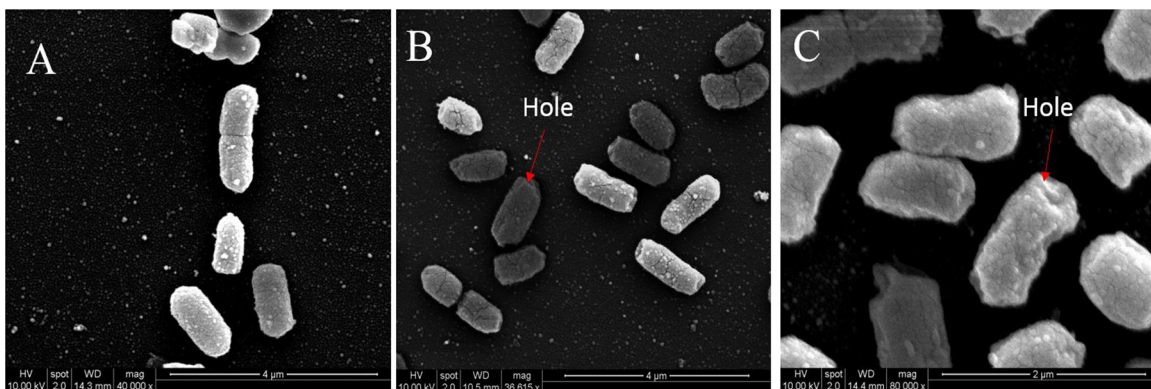


Fig. 3. SEM images of *E. coli* K-12 with photocatalytic inactivation treatment by NP600 for (A) 0 h, (B) 2 h, (C) 4 h.

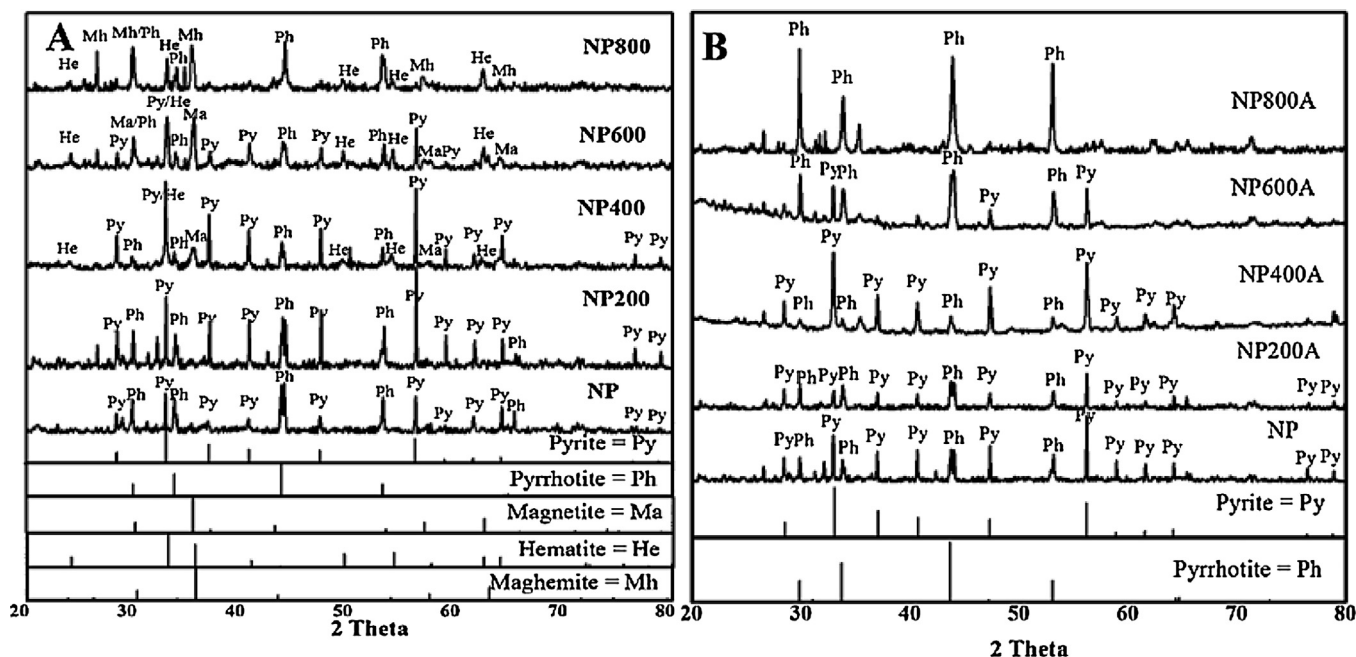


Fig. 4. XRD spectra of annealed NP in (A) air and (B) argon.

absent in intact *E. coli* with well-preserved cell envelope, indicating oxidative damage to the cell. In comparison, most cells retained intact envelope treated with NP even after 4 h (data not shown). Unquestionably, the considerable more severe damages to the cell structure are related to the more powerful oxidation stress from the ROSs produced by NP600.

### 3.2. Mechanism of elevated activity for annealed NP

Considering the complexity of pristine NP, the phase transformation and structure reconstruction should be the main reasons leading to the enhanced VL absorption and photocatalytic activity. To collectively illustrate this effect, (1) a series of instrumental analyses were conducted to reveal the mineralogical changes of NP annealed at different temperatures; and (2) a scavenger study was conducted to determine the alteration roles of reactive species induced by these physic-chemical changes in annealed NP.

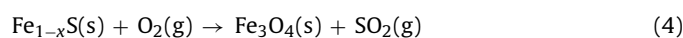
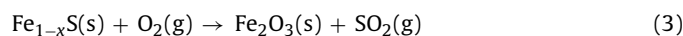
#### 3.2.1. In air

From Fig. 1A, the pristine NP sample was composed with two phases, pyrrhotite and pyrite. The sample showed a deep brown color and the UV–vis absorption tail was found to be at about 465 nm (Fig. 1D). The optical band gap of NP sample was estimated to be about 2.23 eV, which was higher than sole iron sulfide such as pure FeS<sub>2</sub> (0.95 eV). The enlarged band gap could be attributed to the well hybrids of wider gaps impurities like CdS (3.24 eV) or ZnS (3.4 eV) [28] etc. As for NP200, better crystalline of pyrrhotite/pyrite (Fe<sub>1-x</sub>S/FeS<sub>2</sub>) heterojunction with intensified peaks were obtained (Fig. 4A), which facilitated the electron-hole separation and resulted in elevated inactivation efficiency. When the temperature increased to 400 and 600 °C, the sudden appearance of magnetite (Fe<sub>3</sub>O<sub>4</sub>, PDF 19-0629) and hematite (α-Fe<sub>2</sub>O<sub>3</sub>, PDF 33-0664) phases along with pyrrhotite and pyrite formed a complicated composite semiconductor (Fig. 4). Notably, the modified NP displayed obvious red shift with a broader VL absorption shoulder than the pristine NP (Fig. S4A). The integral VL absorbance of NP600 evidently increased by about 50% compared with pristine NP, mainly due to the occurrence of wider band gap hematite (2.2 eV). Therefore, the activity improvement can be attributed to

the replacement of Fe<sub>1-x</sub>S/FeS<sub>2</sub> heterojunction with the formation of Z-scheme composite by coupling FeS<sub>2</sub> with Fe<sub>2</sub>O<sub>3</sub> as shown in Fig. 5. The conduction band (CB) of Fe<sub>2</sub>O<sub>3</sub> (+0.28 eV) is more positive than that of FeS<sub>2</sub> (-0.53 eV) and more negative than the valence band (VB) of FeS<sub>2</sub> (+0.42 eV), thus allowing photogenerated electrons transfer from the CB of FeS<sub>2</sub> to the CB of Fe<sub>2</sub>O<sub>3</sub> and then to the VB of FeS<sub>2</sub> after VL activation. The energy band configuration of this Z-scheme photocatalyst system could significantly promote the separation efficiency of photogenerated electron-hole pairs [29,30], and therefore improve the inactivation efficiency. Additionally, some reports suggested that calcination at high temperatures and with a fast heating rate could produce oxygen or sulfur vacancies in the mineral structure [31,32]. These vacancies could act as electron traps and also prohibit electron-hole recombination.

As for NP800, hematite and maghemite (γ-Fe<sub>2</sub>O<sub>3</sub>, PDF 39-1346) became the major components and pyrite was totally disappeared (Fig. 4A). Correspondingly, the UV–vis absorbance of NP800 obviously decreased (Fig. S4A). Moreover, the mineral particles of NP800 were observed to form a tightly sintered compact (as shown in Fig. S5) with remarkably decreased surface area, which might also influence the photocatalytic reactivity.

In air, magnetite and hematite were the mainly thermal transformed products. The proportions of each constituent mineral phase changed with the heating temperature were calculated and shown in Fig. S6A. Therefore, the thermal process can be described by the following reactions based on above results and discussion [18,19,33]:



#### 3.2.2. In argon

In argon atmosphere, pyrrhotite and pyrite were still the dominant mineral phases in NP200A and NP400A (Fig. 4B). As the temperature increased to 600 °C, the phase proportion of pyrrhotite increased and exceeded pyrite (Figure S6B), indicating pyrite was partially decomposed and transformed to pyrrhotite (Fig. 4B). Such

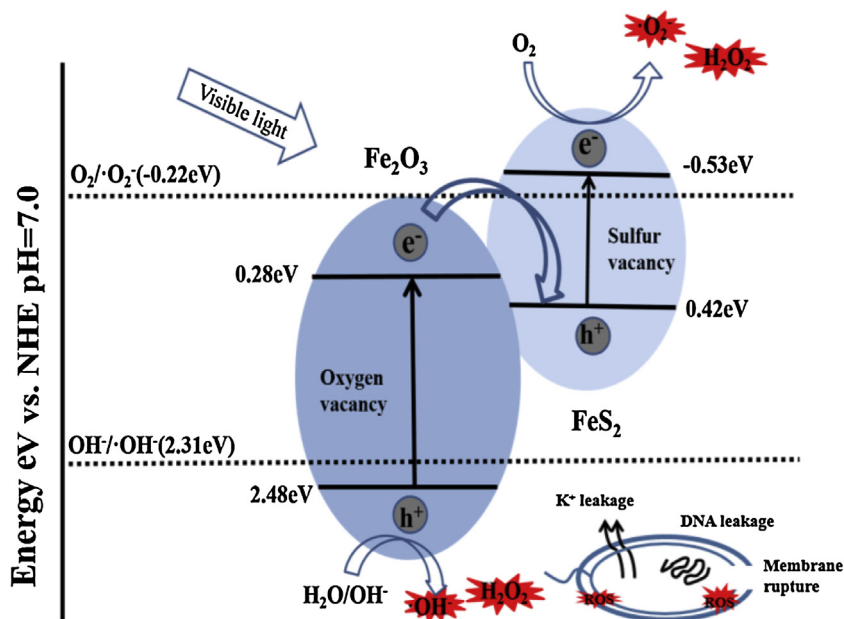


Fig. 5. Schematic diagram of the energy band configuration of  $\text{FeS}_2/\text{Fe}_2\text{O}_3$  heterojunction and separation of electron-hole pairs at the interface under light irradiation.

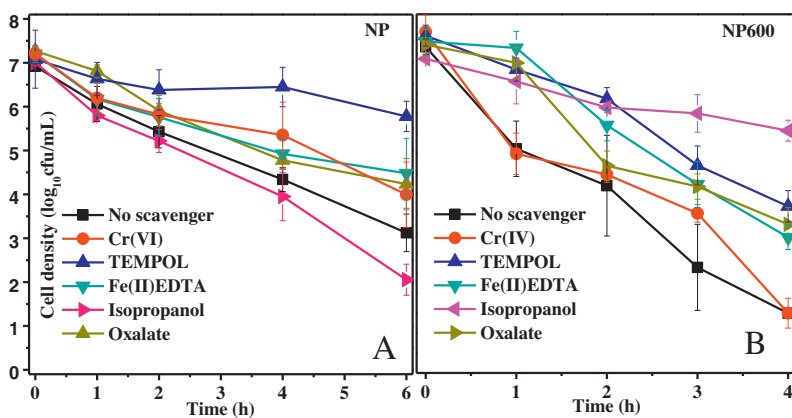


Fig. 6. Photocatalytic inactivation efficiencies with chemical scavengers (Fe-EDTA, 0.1 mM; Cr(VI), 0.05 mM; TEMPOL, 1 mM; sodium oxalate, 0.5 mM; isopropanol, 0.5 mM) in the presence of (A) NP and (B) NP600.

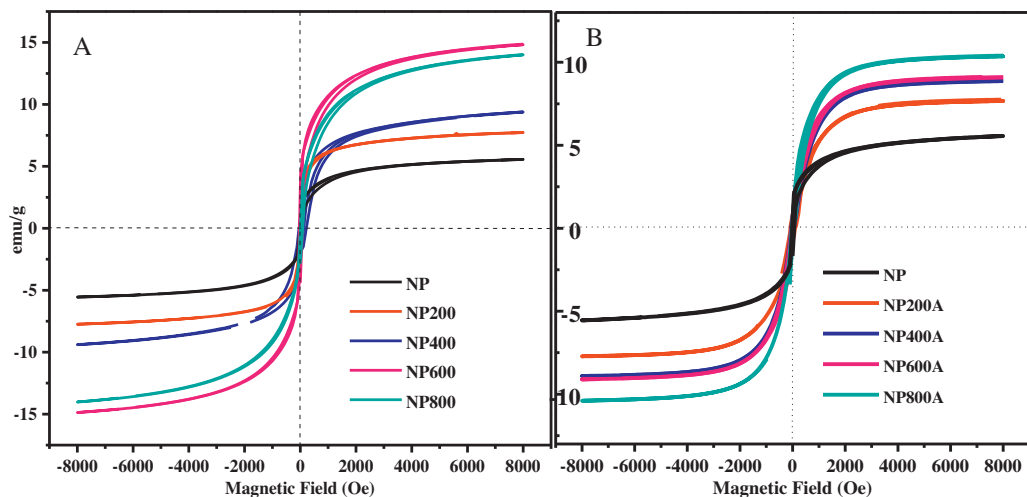


Fig. 7. Magnetic hysteresis curves of annealed NP in (A) air and (B) argon.

a transformation resulted in a slight enhancement of VLD photocatalytic efficiency when compared to the pristine and other thermally treated NP samples (Fig. 2B). So, it can be estimated that increasing the phase ratio of pyrrhotite in pyrrhotite/pyrite heterojunction would improve the photocatalytic activity. Correspondingly, the UV–vis spectra of NP400A and NP600A showed stronger VL adsorption at wavelengths longer than 500 nm (Fig. S4B). However, further increasing the heating temperature resulted in the succeeding transformation of pyrite to pyrrhotite. And there was only one mineral phase of pyrrhotite left in NP800A (Fig. 4B). Since pyrrhotite is a narrow band gap (0.1 eV) semiconductor and the heterojunction of pyrrhotite/pyrite disappeared, the VLD photocatalytic inactivation performance of NP800A should be weakened, which was consistent with the photocatalytic experimental results (Fig. 2B).

In argon, the continuous decomposition of pyrite and formation of pyrrhotite was observed, which was also indicated by the variations of phase proportion shown in Figure S6B. So, the thermal reaction occurred in argon could be represented by Eq. (5).



### 3.2.3. Variation of primary reactive species

When annealing NP in air, the original iron sulfides partially transformed to iron oxides, which would result in the variation of ROSs in bacterial inactivation reactions. Mechanisms of bactericidal function from various ROSs has been well-documented:  $\bullet\text{OH}$  and  $\bullet\text{O}_2^-$  with powerful oxidative ability were suggested to attack cell directly; and  $\text{H}_2\text{O}_2$  can diffuse into inner part of the bacterial cell to produce a long-range inactivation effects, and then followed by the increase in the cell envelope permeability and ROSs penetration into cytoplasm, and ultimately caused the cell death [4,24,34]. Therefore, scavenger experiments [4,34] were conducted to identify the differences of primary bactericidal agents between pristine NP and the most effective NP600. Before the experiments, the concentration of each scavenger reagent was optimized to avoid the possible toxicity to cells. And the results shown in Fig. S7 indicated the concentration of each scavenger reagent used in our experiments couldn't cause any obvious loss of cell density within 6 h.

For pristine NP (Fig. 6A), the cell inactivation was almost totally suppressed in the presence of 1 mM TEMPOL and 0.1 mM Fe(II)-EDTA. Since TEMPOL and Fe(II)-EDTA could effectively quench most of  $\bullet\text{O}_2^-$  and  $\text{H}_2\text{O}_2$ , respectively, the results indicated that photogenerated  $e^-$  (precursor of  $\bullet\text{O}_2^-$  and  $\text{H}_2\text{O}_2$ ) played an important role in bacterial inactivation. Consistently, the use of 0.05 mM Cr(VI) as an  $e^-$  scavenger resulted in poorer inactivation performance, because it inhibited the ROSs ( $\bullet\text{O}_2^-$  and  $\text{H}_2\text{O}_2$ ) producing pathway. Theoretically, the reduction potentials of CB ( $-0.53$  eV) electrons in pyrite ( $\text{FeS}_2$ ) was negative enough to reduce  $\text{O}_2$  into  $\bullet\text{O}_2^-$  ( $-0.23$  eV), whereas the oxidation potential of VB holes ( $+0.42$  eV) were incapable to oxidize  $\text{H}_2\text{O}/\text{OH}^-$  into  $\bullet\text{OH}$  ( $+2.38$  eV) [35]. No involvement of  $\bullet\text{OH}$  was evidenced by the observation that no discrepancy occurred between with or without the addition of  $\bullet\text{OH}$  scavenger (0.5 mM isopropanol). However, without the function of  $\bullet\text{OH}$ ,  $h^+$  was still preferable to directly attack the bacteria, which was confirmed by the suppressing performance with the addition of 0.5 mM oxalate. These results revealed that CB electrons played the most critical role in bacterial inactivation.

However, as for NP600 (Fig. 6B), a remarkable inhibition of the cell inactivation was observed when  $\bullet\text{OH}$  was removed by 1 mM isopropanol, indicating its significant bactericidal role. This was further confirmed by the oxalate addition, as the inactivation was also highly depressed by eliminating  $\bullet\text{OH}$  precursors of VB  $h^+$ . While, when Cr(VI) was added to remove CB  $e^-$ , the inhibition of cell inactivation was also observed, indicating the photogenerated  $e^-$  or its derivatives were involved in the photocatalytic bactericidal reaction. Unquestionably,  $\bullet\text{O}_2^-$  and  $\text{H}_2\text{O}_2$  should also be the

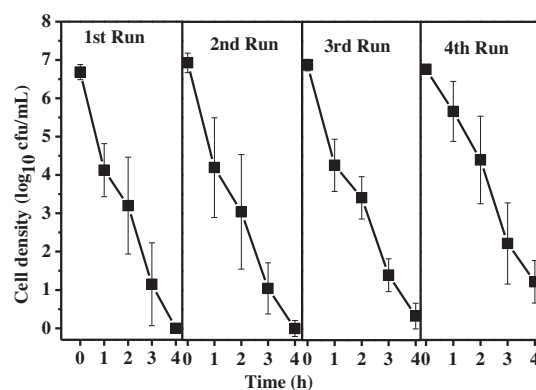


Fig. 8. Repeated experiments of photocatalytic inactivation of *E. coli* K-12 ( $2 \times 10^7$  cfu/mL, 50 mL) by recycled NP600 under light irradiation.

primary bactericidal agents, which was evidenced by the great inhibition of bacterial inactivation when TEMPOL and Fe(II)-EDTA were added. Thus, different from the pristine NP, the powerful species for the bacterial inactivation were generated from both VB and CB of NP600. The discrepancy of ROSs producing pathways between pristine NP and NP600 confirmed the formation of Z-scheme heterojunction composite ( $\text{FeS}_2\text{-Fe}_2\text{O}_3$ ). In such case, the VB  $h^+$  of  $\text{FeS}_2$  could efficiently capture the CB  $e^-$  of  $\text{Fe}_2\text{O}_3$  to promote the separation of  $e^-h^+$  pairs, and the VB  $h^+$  of  $\text{Fe}_2\text{O}_3$  ( $+2.48$  eV) could oxidize  $\text{OH}^-/\text{H}_2\text{O}$  ( $(E^0(\text{OH}^-/\bullet\text{OH})) = +2.38$  V vs NHE) [36], giving rise to  $\bullet\text{OH}$  responsible for bacterial inactivation.

### 3.3. Elevated magnetic property of annealed NP

Mainly due to the existence of ferromagnetic pyrrhotite [37], pristine NP showed a saturation magnetization of approximately 5 emu/g (Fig. 7). Hysteresis loops in Fig. 7 revealed how the curves change with the formation of new phases after NP was annealed. For NP200, the increased phase proportion of pyrrhotite (Fig. S6A) induced slight increase of the magnetization to 7.5 emu/g. The saturated magnetization value rapidly increased to 9.5 emu/g for NP400 and to 15 emu/g for NP600, mainly due to the appearance of magnetite and maghemite [38–40]. As for NP800, the ferromagnetic property slightly decreases to 14 emu/g because magnetite was further oxidized into antiferromagnetic hematite with a negligible saturation magnetization of 0.57 emu/g [41,42].

While in argon atmosphere, the saturation magnetization of thermally treated samples increased from 5 to 10 emu/g with the rising temperature (Fig. 7), mainly due to the continuing production of pyrrhotite (Figure S6B). Importantly, reports have mentioned that the magnetic recovery efficiency would be increased with the enhancement of the material magnetization. So, the enhanced magnetic properties will have important implications for ease separation of photocatalysts from liquid reaction systems.

### 3.4. Enhanced stability of annealed NP

Interestingly, all the used NP can be easily separated and recycled with a magnetic field. Thus the stability of the most effective NP600 was investigated by repeating photocatalytic inactivation experiments with recycled samples. Before another run, samples were washed twice with distilled water after each reaction. NP600 maintained excellent photocatalytic activity with only slight decrease from the fourth run (Fig. 8). The slight decrease in the fourth run was possibly due to the weight loss of the minerals during the recycling procedures.

Besides, photocorrosion may also cause secondary metallic pollution therefore going against the utilization of natural mineral. In

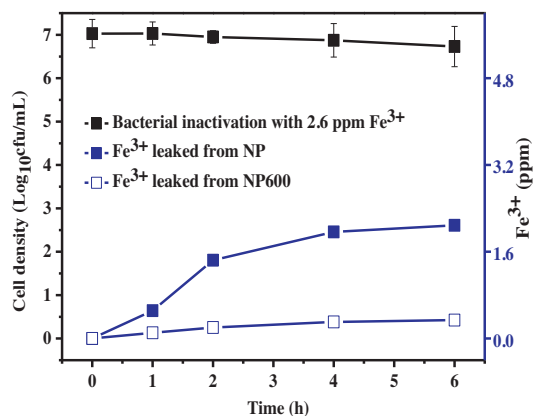


**Fig. 9.** Iron ion ( $\text{Fe}^{3+}$ ) bleed from 50 mg/L pristine NP and NP600 suspension and its bactericidal effect under light irradiation.

this study, when pristine NP was used as the VLD photocatalyst, only a little amount of  $\text{Fe}^{3+}$  (2.6 mg/L is none toxic to cells) can be detected by AAS after 4 h experimental duration (Fig. 9). As the photocorrosion occurred to such a minor extent, the photostability of pristine NP is considerably good. In comparison, the elution amount of Fe ion from NP600 was almost undetectable with a value of 0.084 mg/L, indicating the photostability was greatly enhanced after thermal treatment. All above results supported the calcinations helped to increase the photoactivity, maintain the good stability, and enhance the magnetic property of pristine NP.

#### 4. Conclusions

In summary, a novel mineral material was developed for the photocatalytic inactivation of bacterial cells by using thermally treated NP as the photocatalyst. The results indicated that thermal treatment could remarkably enhance the photocatalytic activity and stability of NP. In good accordance with the newly formed  $\text{Fe}_2\text{O}_3\text{-FeS}_2$  composite, the dominant bactericidal species was changed from  $\cdot\text{O}_2^-$  for pristine NP to  $\cdot\text{OH}$  for NP600. Besides, NP600 with better photostability was found to be able to maintain higher photoactivity for several recycling use. Our findings here provided a new insight into the development of natural semiconductor minerals for cost-effective environmental application.

#### Acknowledgements

The project was supported by General Research Fund (GRF476811) of Research Grant Council and ITSP Tier 3 Scheme (ITS/273/13) of Innovation Technology Commission, Hong Kong SAR Government to P.K. Wong, National Natural Science Funds for Distinguished Young Scholars (41425015) to T.C. An, National Science Foundation of China (21077104) to G.Y. Li, and National Basic Research Program of China (973 Program) (2014CB846001) and National Natural Science Foundation of China (41230103 & 41272003) to A.H. Lu and Y. Li. P.K. Wong also thanks the support from CAS/SAFEA International Partnership Program for Creative Research Teams of Chinese Academy of Sciences, China.

#### Appendix A. Supplementary data

Supplementary data associated with this article can be found, in the online version, at <http://dx.doi.org/10.1016/j.apcatb.2015.04.024>

#### References

- [1] Y. Li, A.H. Lu, S. Jin, C.Q. Wang, J. Hazard. Mater. 170 (2009) 479–486.
- [2] Y. Li, A.H. Lu, C.Q. Wang, Acta Geol. Sin. 80 (2006) 267–272.
- [3] Y. Li, A.H. Lu, C.Q. Wang, X.L. Wu, Sol. Energy Mater. Sol. Cells 92 (2008) 953–959.
- [4] Y.M. Chen, A.H. Lu, Y. Li, L.S. Zhang, H.Y. Yip, H.J. Zhao, T.C. An, P.K. Wong, Environ. Sci. Technol. 45 (2011) 5689–5695.
- [5] D.H. Xia, T.W. Ng, T.C. An, G.Y. Li, Y. Li, H.Y. Yip, H.J. Zhao, A.H. Lu, P.K. Wong, Environ. Sci. Technol. 47 (2013) 11166–11173.
- [6] Y.H. Liu, L. Meng, L. Zhang, Thin Solid Films 479 (2005) 83–88.
- [7] X.Y. Chen, Z.H. Wang, X. Wang, J.X. Wan, J.W. Liu, Y.T. Qian, Inorg. Chem. 44 (2005) 951–954.
- [8] M.L. Kang, F.R. Chen, S.J. Wu, Y.Q. Yang, C. Bruggeman, L. Charlet, Environ. Sci. Technol. 45 (2011) 2704–2710.
- [9] S.K. Bhar, S. Jana, A. Mondal, N.J. Mukherjee, Colloid. Interface Sci. 393 (2013) 286–290.
- [10] S.J. Bae, D.W. Kim, W.J. Lee, Appl. Catal. B: Environ. 134–135 (2013) 93–102.
- [11] K.J. Edwards, P.L. Bond, T.M. Gihring, J.F. Banfield, Science 287 (2000) 1796–1799.
- [12] M.A. Shannon, P.W. Bohn, M. Elimelech, J.G. Georgiadis, B.J. Marinas, A.M. Mayes, Nature 452 (2008) 301–310.
- [13] Y.B. Luan, L.Q. Jing, J. Wu, M.Z. Xie, Y.J. Feng, Appl. Catal. B: Environ. 147 (2014) 29–34.
- [14] T.K. Le, D. Flahaut, H. Martinez, H.K.H. Nguyen, T.K.X. Huynh, Appl. Catal. B: Environ. 165 (2015) 260–268.
- [15] M.A. Aramendia, V. Borau, J.C. Colmenares, A. Marinas, J.M. Marinas, J.A. Navio, F.J. Urbano, Appl. Catal. B: Environ. 80 (2008) 88–97.
- [16] T.C. An, J.K. Liu, G.Y. Li, S.Q. Zhang, H.J. Zhao, X.Y. Zeng, G.Y. Sheng, J.M. Fu, Appl. Catal. A: Gen. 350 (2008) 237–243.
- [17] J.K. Liu, T.C. An, G.Y. Li, N.Z. Bao, G.Y. Sheng, J.M. Fu, Mesopor. Micropor. Mater. 124 (2009) 197–203.
- [18] J.R. Schorr, J.O. Everhar, J. Am. Ceram. Soc. 52 (1969) 351–354.
- [19] S.K. Bhargava, A. Garg, N.D. Subasinghe, Fuel 88 (2009) 988–993.
- [20] A. Ennaoui, S. Fiechter, C. Pettenkofer, N. Alonso-Vante, K. Bükler, M. Bronold, C. Höpfner, H. Tributsch, Sol. Energy Mater. Sol. Cells. 29 (1993) 289–370.
- [21] L. Wang, Y.X. Pan, J.H. Li, H.F. Qin, Sci. China Ser. D. 51 (2008) 1144–1153.
- [22] K.E. Waters, N.A. Rowson, R.W. Greenwood, A.J. Williams, Miner. Eng. 21 (2008) 679–682.
- [23] H.X. Shi, G.Y. Li, H.W. Sun, T.C. An, H.J. Zhao, P.K. Wong, Appl. Catal. B: Environ. 158 (2014) 301–307.
- [24] H.W. Sun, G.Y. Li, X. Nie, H.X. Shi, P.K. Wong, H.J. Zhao, T.C. An, Environ. Sci. Technol. 48 (2014) 9412–9419.
- [25] C.Y. Jia, D.Z. Wei, P.J. Li, X.J. Li, P.D. Tai, W. Liu, Z.Q. Gong, Colloid Surf. B: Biointerf. 83 (2011) 214–219.
- [26] A.H. Geeraerd, C.H. Herremans, J.F. van Impe, Int. J. Food Microbiol. 59 (2000) 185–209.
- [27] F. Bosshard, M. Bucheli, Y. Meur, T. Egli, Microbiology 156 (2010) 2006–2015.
- [28] L. Huang, X.L. Wang, J.H. Yang, G. Liu, J.F. Han, C.J. Li, J. Phys. Chem. C 117 (2000) 11584–11591.
- [29] P. Zhou, J.G. Yu, M. Jaroniec, Adv. Mater. 26 (2014) 4920–4935.
- [30] D.O. Scanlon, C.W. Dunnill, J. Buckeridge, S.A. Shevlin, A.J. Logsdail, S.M. Woodley, C.R.A. Catlow, M.J. Powell, R.G. Palgrave, I.P. Parkin, G.W. Watson, T.W. Keal, P. Sherwood, A. Walsh, A.A. Sokol, Nat. Mater. 12 (2013) 798–801.
- [31] O. Warschkow, D.E. Ellis, J. Hwang, N. Mansourian-Hadavi, T.O. Mason, J. Am. Ceram. Soc. 85 (2002) 213–220.
- [32] M. Birkholz, S. Fiechter, A. Hartmann, H. Tributsch, Phys. Rev. B 43 (1991) 926–936.
- [33] C.J. Goss, Phys. Chem. Miner. 16 (1988) 164–171.
- [34] W.J. Wang, J.C. Yu, D.H. Xia, P.K. Wong, Y.C. Li, Environ. Sci. Technol. 47 (2013) 8724–8732.
- [35] G.V. Buxton, C.L. Greenstock, W.P. Helman, A.B. Ross, W.J. Tsang, Phys. Chem. Ref. Data. 17 (1988) 513–886.
- [36] Y. Kikuchi, K. Sunada, T. Iyoda, K. Hashimoto, A.J. Fujishima, Photochem. Photobiol. A: Chem. 106 (1997) 51–56.
- [37] S.E.J. Male, Phys. D: Appl. Phys. 13 (1980) 67–70.
- [38] S. Nasrazadani, A. Raman, Corros. Sci. 34 (1993) 1355–1365.
- [39] T. Ishikawa, E. Matijevic, Langmuir 4 (1988) 26–31.
- [40] K.E. Waters, N.A. Rowson, R.W. Greenwood, A.J. Williams, Sep. Purif. Technol. 56 (2007) 9–17.
- [41] L. Wang, Y.X. Pan, J.H. Li, H.F. Qin, Sci. China Ser. D. 51 (2008) 1144–1153.
- [42] I. Okada, M. Ozaki, E.J. Matijevic, Colloid Interface Sci. 142 (1991) 251–256.